Effect of temperature and strain rate on the formation of shear bands in polymers under quasi-static and dynamic compressive loadings: Proposed constitutive model and numerical validation

Effect of temperature and strain rate on the formation of shear bands in polymers under quasi-static and dynamic compressive loadings: proposed constitutive model and numerical validation

E. Farotti[1], E. Mancini[2], A. Lattanzi[1], M. Utzeri[1], M. Sasso[1*]

[1]*Università Politecnica delle Marche, DIISM, Via Brecce Bianche, 60121 Ancona.*

[2]*Università degli Studi dell'Aquila, DIIIE, Piazzale Ernesto Pontieri, 67100 L'Aquila.*

**Corresponding author: m.sasso@staff.univpm.it,*

Keywords: constitutive model; shear banding; numerical simulation; polymers

ABSTRACT

The mechanical behaviour of polymers is strongly influenced by temperature and strain rate conditions. Their effects are clearly observed in the Young modulus and Yield strength assessment. In some cases, a change in material failure mode can be noted, which can be both ductile and brittle. For polymers exhibiting shear bands during compression loading, test conditions may enhance or diminish this effect. In this study, isotactic Polypropylene has been considered due to its strong sensitivity to test conditions; with some combinations of strain rate and temperature, the material is able to undergo large compression with nearly uniform strain distribution, whereas significant shear bands can be observed with other strain rate and temperature combinations. This paper proposes a constitutive law for the mechanical characterization of polymers that show shear banding in compression loading. The proposed law extends a visco-plastic model present in literature, allowing to predict the onset or not of micro-shear banding compression instability. The dependence of constitutive parameters with test conditions is determined by applying the Ree-Eyring equation. The model parameters have been calibrated analytically according to experimental data obtained from compression tests performed in a wide range of strain rates (10^{-3} to 10^{3} 1/s) and temperatures (253 to 313 K). In addition, the constitutive model has been implemented in a commercial FEM code by means of a user-defined subroutine. Results show a good correspondence between experimental observations and numerical calculations, regarding both stress-strain relationship and shear band formation.

INTRODUCTION

Polymers are well-known materials having a mechanical behaviour strongly dependent on the test conditions. In fact, small temperature changes or strain rate variations affect the mechanical response. The cause of this variability can be found in the structure of polymers. In general, the relative motion of polymer chains is favoured by an increment of temperature whereas it is harder in the case of rapid deformation. While a deformation is applied, intermolecular interactions take place and prevent the molecular rearrangement, causing an increase in the material resistance. When the strain rate increases, this effect is more pronounced. On the other hand, molecular mobility also depends on temperature, to which the thermal energy of molecules is associated. Therefore, an increment of temperature increases the thermal energy and aids the arrangement of molecular segments [1], with a consequent reduction of resistance.

The effects of these factors are clearly observable on mechanical properties such as Young modulus and Yield stress. In particular, the change in Young modulus can be measured by means of viscoelastic property measurement techniques such as Dynamic Mechanical Analysis (DMA) [2–4] or Molecular Dynamics (MD) [5]. On the other hand, the Yield stress is identified by static and dynamic mechanical tests. Many authors [6–9] studied the relationship between Yield stress, strain rate and temperature, obtaining analytical expressions correlating experimental data. The most commonly used constitutive equations for Yield stress modelling are the two-term power-law, the Ree-Eyring, the cooperative, and modified Eyring equations [10]. In particular, the Ree-Eyring based models are quite common in polymers characterization, because they include both strain rate and temperature. To mention some examples, there are applications for PC, PMMA and PAI in the study by Richeton et al [6], for PEEK in El-Qoubaa and Othman [11], for epoxy resins in Gómez-del Río and Rodríguez [12] and Tamrakar et al [13].

The mechanical behaviour of polymers, after an applied deformation, depends on their internal structure: referring to room temperature and quasi-static conditions, they are classified as brittle (epoxy resins, PS), semi-ductile (PMMA), ductile (PET, PC, PP) or elastomeric (urethane) [14]. When commonly ductile polymers are subjected to dynamic loads it is sometimes possible to observe a ductile-brittle transition, as in the studies of Li and Lambros for PMMA [15], Plaseied and Fatemi for vinyl ester resin [16], Brown et al for PCTFE [17], etc. The material can still exhibit a ductile response at high temperatures in the dynamic range. This behaviour is typically reported in fracture studies, such as those of Newmann and William on ABS [18], Gaymans et al. on PC [19], Kitao on LDPE, LLDPE, MDPE, and HDPE [20].

Some polymers exhibit unique rupture mechanisms when subjected to compression loads. Shear bands are one of the most frequently observed in the literature. In particular, when glassy polymers undergo large plastic deformations, inhomogeneity and strain localization occur [21]. This phenomenon causes the material to become unstable and lose its mechanical ability to withstand an applied load. In addition, some investigators have reported the dependence of the shear bands occurrence on external conditions such as ambient temperature [22] and strain rate [23]. At high strain rate tests the plastic deformation work is converted into heat and is internally dissipated. This happens because of the very low thermal diffusivity of polymers compared to metals (10^{-7} m^2/s vs 10^{-4} m^2/s respectively) [24]. In this case, the test is adiabatic, and heat determines an increase in specimen temperature that can lead to a localized failure of the material. Reasoning by orders of magnitude, a polymeric specimen of 10 mm length should be subjected to a strain rate higher than 10^{-3} 1/s to ensure adiabatic conditions. This means that only under quasi-static test conditions the material is in isothermal state. Therefore, in the dynamic regime, this failure mechanism is commonly known as Adiabatic Shear Bands (ASB).

A unique position regarding the effective mechanisms of shear band formation is absent in the literature. At first, these bands were commonly assumed as a form of instability caused by thermal softening effects (induced by adiabatic plastic work) dominating the strain and strain rate hardening ones. Conversely, new assumptions have been carried out in metals, as in Medyanik et al. [25] and Rittel [26], where ASB are considered a microstructural rearrangement caused by dynamic recrystallization (DRX) occurring at the onset of deformation. Since polymeric materials are strongly sensitive to temperature changes, and high rate loadings can be considered adiabatic, thermal softening is the main cause of possible unstable growth of localised shear bands [27].

The formation criteria for ASB have been widely discussed in the literature, mainly following two kinds of approach [25]. In the former, an analytical solution for the description of the propagation of shear bands is derived from momentum and energy balances, as in Wright [28], but only through model approximations. The second approach found more application since it is based on the simulation of shear banding by constitutive equations capable of highlighting this phenomenon in thermo-mechanical numerical models. An advantage of this method is the possibility of studying the formation and propagation of ASB. Based on this approach, the material constitutive model has a local maximum in the flow curve, induced by the temperature softening effect [27, 29].

This paper shows an analysis of the effects of temperature and strain rate on the adiabatic shear banding of polymers that undergo compressive loading. In particular, the present work has been conducted on an injection moulded Polypropylene. The study focuses on the implementation of a

constitutive model to assess the experimental findings. Polypropylene exhibited a significant dependence of its properties on varying test conditions, both in terms of stiffness and strength. In addition, experimental results revealed a ductile-to-brittle transition of the mechanical response and the formation of shear bands as the main failure mechanism. The proposed constitutive model considers both the formation of shear bands and the variation of the mechanical properties of the material with strain rate and temperature. This last was integrated into the model by calibrating the Ree-Eyring equation on Yield stress and Young modulus. A numerical model of the compression test has been employed as a validating method of the constitutive law for ASB prediction.

EXPERIMENTAL PROCEDURE

The material used in the experiments is an isotactic Polypropylene (iPP, Borealis®-HF136MO), by which cylindrical specimens (D = L = 10 mm) for compression tests have been manufactured by the injection molding process [30]. Samples have been obtained by different molding process conditions [31]; however, in this work only those obtained at 75 °C of mold temperature have been taken into account.

Compression tests have been performed at different strain rates and temperatures, ranging from 10^{-3} to 10^{3} 1/s and from 253 to 313 K, respectively. Quasi-static tests have been carried out using a standard electromechanical machine (model Zwick/Roell® Z050) at two different crosshead speeds, i.e. 0.6 mm/min and 600 mm/min. Specimen's displacement has been measured by means of a mechanical contacting extensometer, whereas the applied force has been measured with a 50 kN load cell. Dynamic tests have been performed by means of a Split Hopkinson Bar, a machine commonly used for material testing in tension/compression [32–34]. In this study, titanium alloy (Ti6Al4V) bars have been used to achieve high strain rates. The test speed has been set by adjusting the preload in the pre-stressed bar, whereas specimen's strain rate and stress have been calculated from the bars' strain signals acquired with strain gauges. The temperature has been set by hot or cold air jets using Vortec® airguns. Dynamic tests have also been recorded by means of a high-speed camera, model Photron® SA4 at 100 kfps. More details on the adopted Hopkinson bar system and temperature control are reported in Appendix 1.

Strain rate and temperature ranges have been divided into 4 levels, and a full factorial DOE plan with 4^2=16 tests has been carried out.

Table *1* shows the parameter values of each DOE level.

Table 1 – Levels of the full factorial 2-parameters DOE table

	Levels			
	1	2	3	4
***Strain Rate* [s^{-1}]**	10^{-3}	10^{0}	10^{2}	10^{3}
***Test Temperature* [K]**	253	273	293	313

ANALYSIS OF EXPERIMENTAL RESULTS AND OBSERVATIONS

Effects of strain rate and temperature on mechanical properties of iPP

As already presented in the aforementioned paper [31], the mechanical behaviour of iPP is highly dependent on strain rate and temperature conditions. The first aspect to notice is the different material response to strain rate. In fact, the material passes from ductile to brittle behaviour as strain rate increases, as shown in Figure 1. On the other hand, the temperature has the opposite effect, and in the case of 40 °C no brittle failure is observed during tests (Figure 2).

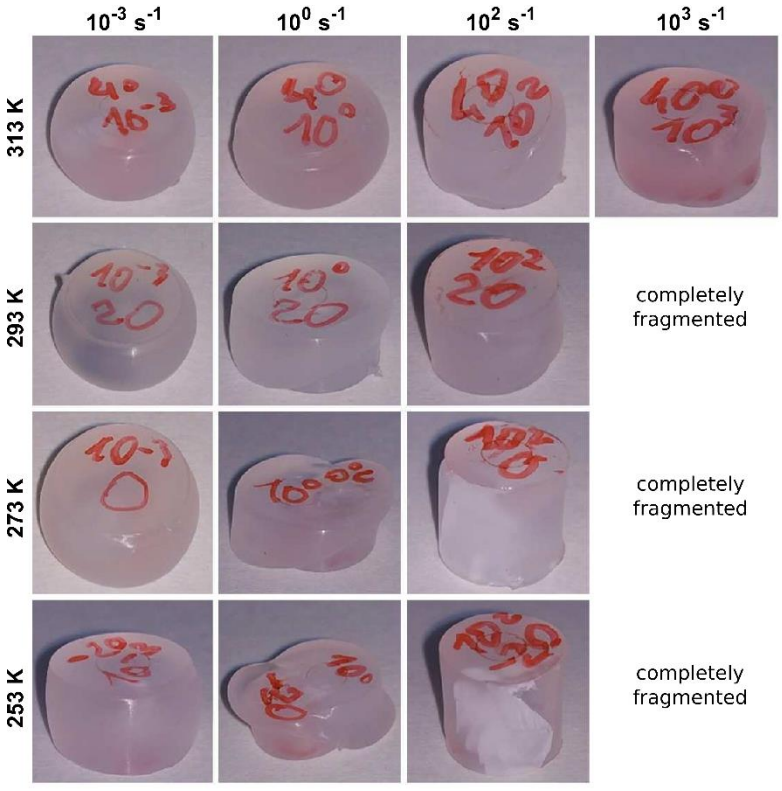

Figure 1 - Specimens after compression test

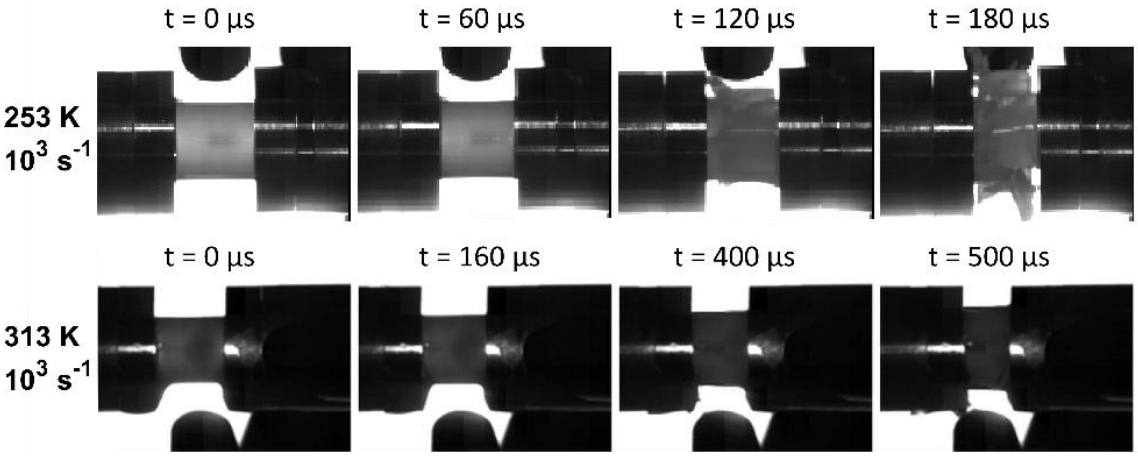

Figure 2 - Temperature effect on the failure behaviour of iPP (the video of the test at 253K 10^3 s^{-1} can be found in the supplementary material)

The results of the compression tests are reported in Figure 3a and Figure 3b, in terms of engineering and true stress-strain curves, respectively. The true data were computed from the engineering ones in the simplified hypothesis of constant volume and uniform deformation. The experimental curves show that, for each temperature level, the strain rate influences both the material stiffness and the Yield point; note that the latter is intended here as the value obtained at the end of the linear-elastic portion of the curve, while the ISO 527 standard defines the yield as the peak stress. During quasi-static tests, no specimen failure was observed, and hence the ultimate strain refers to test interruption. On the contrary, the material response in dynamic tests is brittle, except for the 313 K case, and the failure strain decreases with increasing strain rate. When the material remains ductile under dynamic conditions, the maximum strain reached is dependent on the maximum available stroke in the Hopkinson bar test. In general, the main effect of temperature is the lowering of both Young modulus and Yield strength. In addition, the curves in Figure 3 show a marked fall in material stress at high specimen strains, despite compression conditions, suggesting the occurrence of a material internal failure, which will be discussed in the following sections. The experimental values of Young modulus and Yield stress are summarized in Table 2. The crosshead speed has been reported for quasi-static tests, whereas the initial impact velocity has been considered for dynamic ones. It should be pointed out that the strain rate is not constant in the dynamic tests, hence only the order of magnitude has been reported.

a)

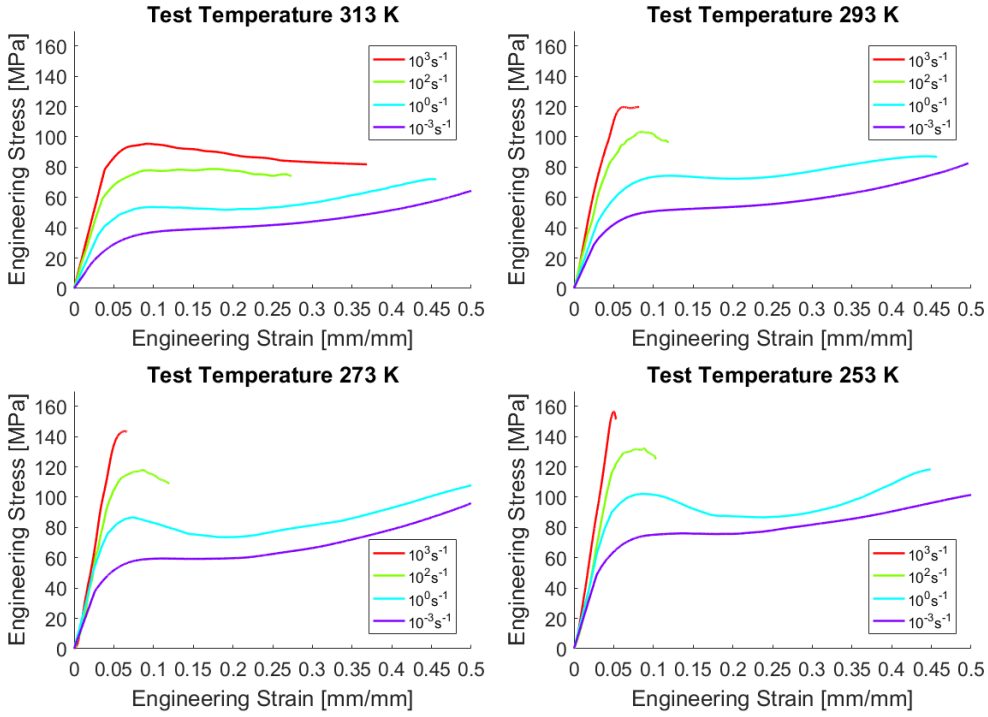

b)

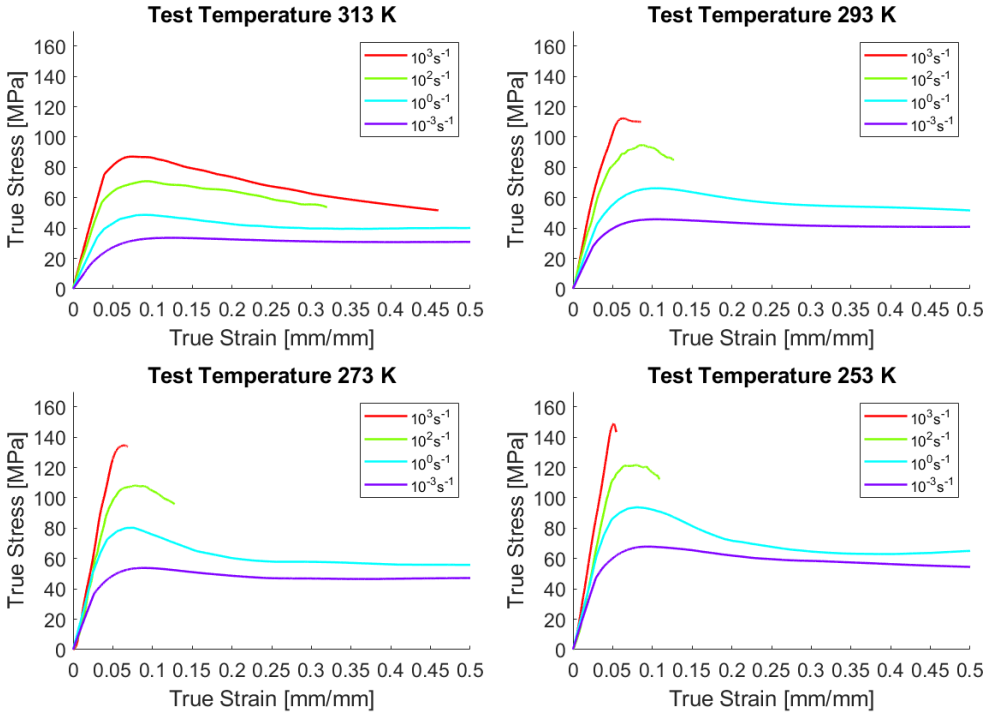

Figure 3 - Stress-strain curves at different temperature and strain rates: a) engineering; b) true

Table 2 - Elastic modulus (E) and Yield strength (σ_y) at different strain rates and temperatures

	253 K		273 K		293 K		313 K	
$\dot{\varepsilon}$ [1/s]	E [MPa]	σ_y [MPa]	E [MPa]	σ_y [MPa]	E [MPa]	σ_y [MPa]	E [MPa]	σ_y [MPa]
10^{-3}	1706.8	48.32	1450.1	38.28	1151.2	28.71	775.9	19.60
10^{0}	2079.4	63.56	1836.7	56.21	1479.7	44.84	1169.3	35.82
10^{2}	2810.2	106.5	2322.6	87.13	2004.2	73.62	1705.1	58.23
10^{3}	3273.6	148.6	2865.4	132.0	2515.8	105.5	2038.2	78.21

Application of Ree-Eyring model for modelling the elastic properties of iPP

The time-temperature dependent behaviour of polymers is often described by the so-called Time-Temperature Superposition principle (TTS), especially in the case of viscoelasticity [14]. Such phenomenological approach has been successfully applied also in describing the large deformations of transparent polyurethane at intermediate [35] and high strain rate [36]. From a physically-based point of view, polypropylene deformation is known to involve two relaxation processes (referred to as α and β) in the deformation mechanisms of the material; this behaviour can be effectively described by the Ree-Eyring model [10], which has been adopted in this work. It is assumed that Yield stress is characterized by the occurrence of multiple processes and that it can be calculated additively for each contribution [37]:

$$\sigma_y = \sigma_y^{\alpha} + \sigma_y^{\beta} \tag{1}$$

where $\sigma_y^{\alpha} = A_{\alpha} T \left(\ln(2C_{\alpha}\dot{\varepsilon}) + \frac{Q_{\alpha}}{RT} \right)$ and $\sigma_y^{\beta} = A_{\beta} T \sinh^{-1}\left(C_{\beta}\dot{\varepsilon} e^{\frac{Q_{\beta}}{RT}} \right)$. Although this model is generally applied for Yield stress characterization [38–40], in this work its application is also assumed for the Young modulus. Hence, the following equations are used to correlate these characteristics depending on the strain rate and temperature:

$$\sigma_y = A_{\alpha y} T \left(\ln(2C_{\alpha}\dot{\varepsilon}) + \frac{Q_{\alpha}}{RT} \right) + A_{\beta y} T \sinh^{-1}\left(C_{\beta}\dot{\varepsilon} e^{\frac{Q_{\beta}}{RT}} \right) \tag{2a}$$

$$E = A_{\alpha E} T \left(\ln(2C_{\alpha}\dot{\varepsilon}) + \frac{Q_{\alpha}}{RT} \right) + A_{\beta E} T \sinh^{-1}\left(C_{\beta}\dot{\varepsilon} e^{\frac{Q_{\beta}}{RT}} \right) \tag{2b}$$

In these equations the terms Q_{α}, Q_{β} represent the activation energies of α,β-relaxations, R is the universal gas constant, σ_y the Yield stress and E the Young modulus at a specific temperature T.

The parameters $A_{\alpha y}, C_{\alpha}, A_{\beta y}, C_{\beta}$ are here considered as material constants but have also a physical interpretation in accordance with the Ree-Eyring theory.

Since the values of $C_{\alpha}, C_{\beta}, Q_{\alpha}, Q_{\beta}$ have already been identified in [31], here they are assumed as known terms. The determination of $A_{\alpha y}, A_{\alpha E}, A_{\beta y}, A_{\beta E}$ coefficients has therefore been obtained by correlating the data of Table 2 using equations (2a) and (2b), through the minimization of a Root Mean Square (RMS) error function. Calibration results are shown in Figure 4a and Figure 4b. Note that while the figure labels show the rounded strain rate decade for the sake of readability, the Ree-Eyring model was calibrated using the actual average strain rates measured in the tests (i.e. the average of strain rate computed with equation A2, converted into true strain rate). The values of the calibrated coefficients are shown in Table 3.

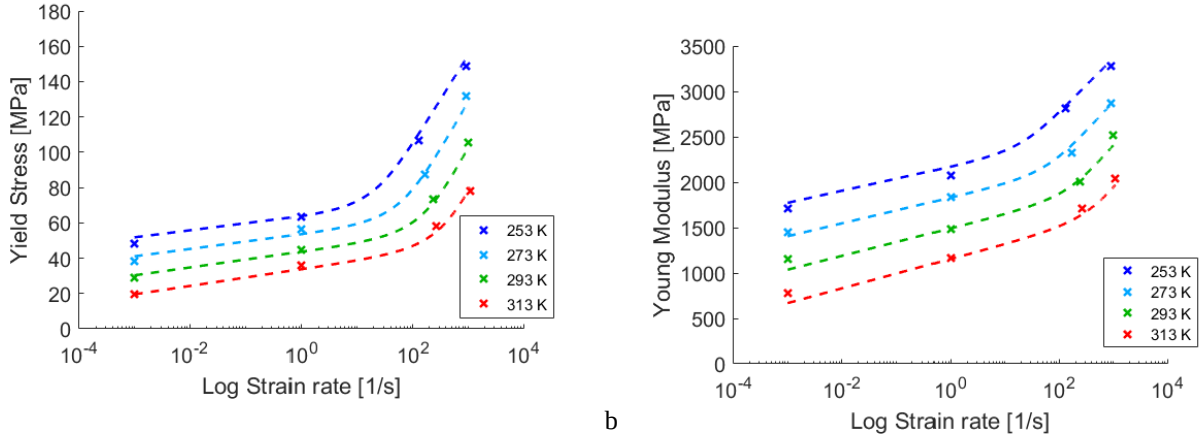

a b

Figure 4 - Ree-Eyring calibration for: a) Yield Stress; b) Young Modulus

Table 3 - Ree-Eyring parameters for iPP

$A_{\alpha y}$ [MPa/K]	$A_{\beta y}$ [MPa/K]	C_{α} [s]	Q_{α} [kJ/mol]
0.0066	0.0799	1.3245e-33	237.78
$A_{\alpha E}$ [MPa/K]	$A_{\beta E}$ [MPa/K]	C_{β} [s]	Q_{β} [kJ/mol]
0.2247	0.8067	8.7202e-09	31.37

The obtained calibration values can be interpreted in the Ree-Eyring theory. In fact, the term σ_y^{α} can be rewritten in accordance with Eyring's expression [41] as:

$$\sigma_y^{\alpha} = \sigma_0^{\alpha} + \frac{k_B T}{V_0^{\alpha}} \ln\left(\frac{\dot{\varepsilon}}{\dot{\varepsilon}_0^{\alpha}}\right) \tag{3}$$

where k_B is the Boltzmann constant, σ_0^{α} is the Yield stress at strain rate $\dot{\varepsilon}_0^{\alpha}$ and V_0^{α} is the activation volume, which is a measure of the scales of the thermally activated process of plastic flow. Comparing the parameters of Table 3 and the terms of Equation (3), it results in the following relationships:

$$A_{\alpha y} = \frac{k_B}{V_0^{\alpha}} \quad ; \quad C_{\alpha} = \frac{1}{2\dot{\varepsilon}_0^{\alpha}} \tag{4}$$

from which it is derived V_0^{α} =2.10 nm^3, $\dot{\varepsilon}_0^{\alpha}$ =3.775 · 10^{32} 1/s. A comparable activation volume is found in the study of Li and Cheung (3 nm^3) [42], while comparable activation energies in those of Porzucek et al. (240 kJ/mol) [43] and Gao et al. (272 kJ/mol) [44].

The second term of Equation (1) becomes significant at high strain rates. Moreover, recalling that for high values of a variable x it is possible to approximate $\sinh^{-1}(x) \approx \ln(2x)$, the expression of yield contribution for β-relaxation becomes formally the same as the first term σ_y^{α}:

$$\sigma_y^{\beta} = A_{\beta} T \sinh^{-1}\left(C_{\beta}\dot{\varepsilon}e^{\frac{Q_{\beta}}{RT}}\right) \approx A_{\beta} T \ln\left(2C_{\beta}\dot{\varepsilon}e^{\frac{Q_{\beta}}{RT}}\right) = A_{\beta} T \left(\ln(2C_{\beta}\dot{\varepsilon}) + \frac{Q_{\beta}}{RT}\right) \tag{5}$$

Hence, it is possible to write:

$$\sigma_y^{\beta} = \sigma_0^{\beta} + \frac{k_B T}{V_0^{\beta}} \ln\left(\frac{\dot{\varepsilon}}{\dot{\varepsilon}_0^{\beta}}\right) \tag{6}$$

where σ_0^{β} is the Yield stress at strain rate $\dot{\varepsilon}_0^{\beta}$ and V_0^{β} is the activation volume, both related to the only β-relaxation mechanism. Similarly, comparing the parameters of Table 3 and the terms of Equation (6), it results in the analogous relationships:

$$A_{\beta y} = \frac{k_B}{V_0^{\beta}} \quad ; \quad C_{\beta} = \frac{1}{2\dot{\varepsilon}_0^{\beta}} \tag{7}$$

from which it is derived V_0^{β} =0.17 nm^3, $\dot{\varepsilon}_0^{\beta}$ = 5.734 · 10^7 1/s.

Shear bands observation

Dynamic compression tests did not allow any optical analysis of the specimens, as they were destroyed or reduced to very small fragments (Figure 5). For an understanding of the failure

mechanism, a displacement control has been set in subsequent trials. Therefore, rings were interposed (Figure 6) to prevent specimens' destruction and to allow optical analysis.

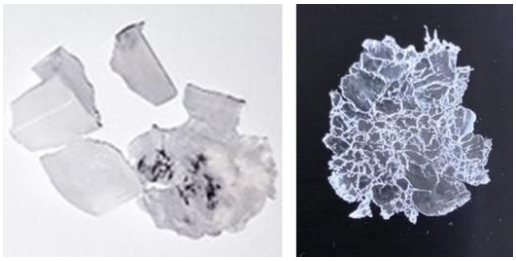

Figure 5 - Specimen after test without bar displacement control

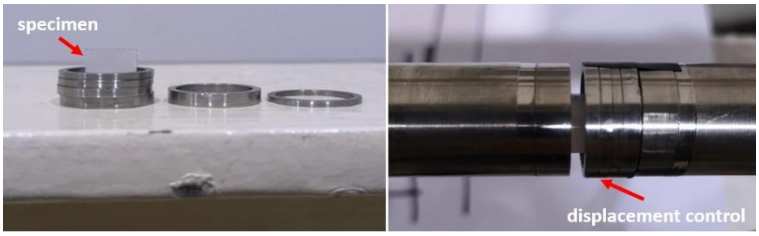

Figure 6 - Bar stroke control system with supporting rings

The analysis of the fracture surfaces has been performed using a Leica DMi8 optical microscope (OM), more details in the methods can be found in [45]. Focusing on Figure 7, it can be noted that the principal direction of rupture is the main shear one. According to Wang et al. [46], the morphology of broken specimen (Figure 5) shows an explosive manner of failure, which can be caused by shear banding and crazing mechanisms [47, 48]. These effects cause a decrease in stress, as shown in the curves of Figure 3, from strain rate 10^0 1/s, where the adiabatic test condition is ensured. Moreover, post-mortem analyses performed with an optical microscope systematically showed the presence of striations and fragments characterized by an angle of approximately 45°, which is an indicator of shear bands; Figure 7 shows an example of specimen failed by shear banding at 273K, 10^2 s^{-1}, partially recomposed after the test.

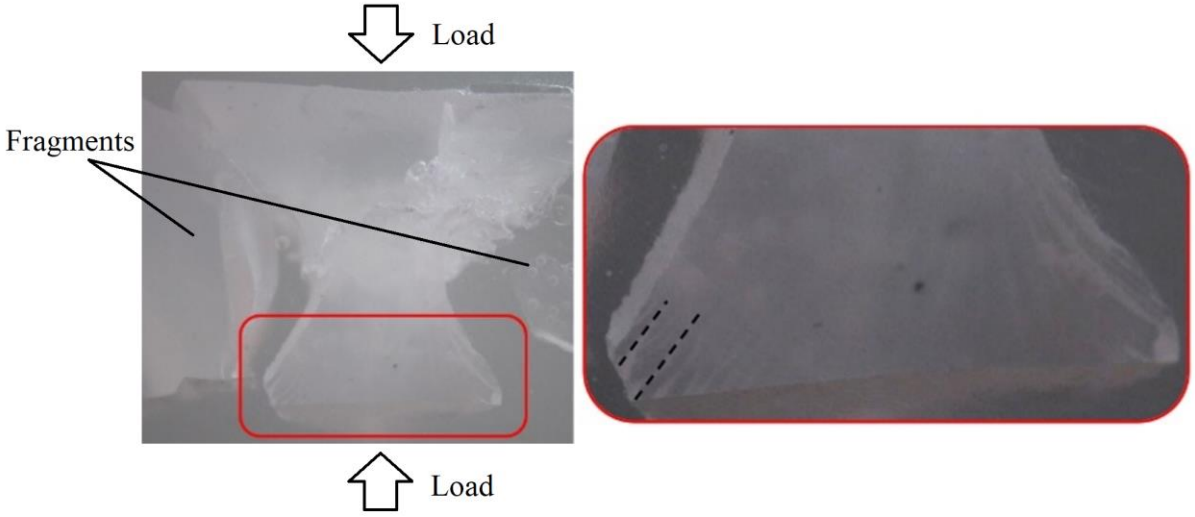

Figure 7 - Specimen failure by compression and shear bands

A MODIFIED CONSTITUTIVE MODEL FOR iPP

A brief recall on constitutive models applied to Polypropylene

In recent years, several complex models have been proposed for Polypropylene, in relation to mechanical loadings or material's microstructure. For instance, O'Connor et al. [49] developed a physically-based model for large displacements, high temperatures and multiaxial stretching of a PP manufactured by thermoforming, calibrating the constitutive parameters by means of biaxial tests in tension. Moreover, studies by Zrida et al. [50] resulted in the development of a phenomenologically-based three-dimensional model for the characterization of tensile and torsional behaviour of an injection-molded Polypropylene. This model was also verified under conditions of cyclic loading and different strain rates.

A common feature of constitutive models for Polypropylene is the description of its elasto-visco-plastic behaviour. In fact, several models can be found in literature, such as those of Drozdov and Gupta [51], Balieu et al. [52] or Okereke and Akpoyomare [53]. The former has been applied to an isotactic polypropylene for injection molding and involves eight parameters connected to the semi-crystalline morphology of the material. The second one determined the constitutive parameters of a mineral filled Polypropylene by means of tensile and compression tests at different strain rates. Conversely, the latter developed a three-dimensional physical-based model for the compression behaviour of the material at different temperatures and across a wide range of strain rates.

The Nowak-Peçherski model

In this paper, a visco-plastic model, considering a micro-shear banding mechanism, has been adopted to evaluate the response of the iPP after deformation. The reasons for this choice are related to the experimental observations described in the previous section and to the similarities found in the literature. Moreover, this behaviour has been observed by other researchers, such as Pieczyska et al. [54] who studied a glass fiber reinforced PP. They used a constitutive model for Polypropylene, based on the work of Nowak and Peçherski [55], who discussed the identification of a shear banding contribution function as a cause of the low hardening in compression of polycrystalline copper.

The model relates the true stress to true plastic strain, in dependence of strain rate, with the following expression:

$$\sigma = \left(1 - \frac{f_{SB_0}}{1 + e^{a - b\varepsilon_p}}\right)\left(A + B\varepsilon_p^n\right)\left[1 + \left(\frac{\dot{\varepsilon}}{\dot{\varepsilon}_0}\right)^D\right] \tag{8}$$

where $(f_{SB_0}, a, b, A, B, n, D)$ are material constants and $\dot{\varepsilon}_0$ is a reference strain rate. In Equation (8), the increase in f_{SB_0} results in a relevant stress softening caused by shear banding, whereas coefficients a and b define the onset point of stress collapse due to instability, modifying both stress and strain. In general, this point is delayed at high values of a and low values of b. The remaining coefficients A, B, n relate to a classical strain hardening described by a power-law function, while $\dot{\varepsilon}_0$ and D are the coefficients of Cowper-Symonds [56] model for the strain rate dependence.

Model modification and calibration

The Ree-Eyring model has been applied to some of the constitutive parameters to predict the behaviour of the material at different temperatures and strain rates. Firstly, the linear elastic part has been replaced by Equation (2b). Then, a proportionality function K_{RE} has been defined as the ratio between the Yield strength given by Equation (2a) and the Yield strength at the reference condition of 293K temperature and 10^{-3} s^{-1} strain rate. This function allows replacing the Cowper-Symonds term valid only for strain rate dependency. Hence, it can be written:

$$\sigma_y = K_{RE}\left(\dot{\varepsilon}, T\right)\sigma_0 \tag{9}$$

In addition, a qualitative analysis of the curves in Figure 3 shows that the drop in resistance after the first peak of the stress-strain curve changes considerably in each test. Thus, the f_{SB_0} factor has

been imposed to vary with the K_{RE} function as well: $f_{SB}(\dot{\varepsilon},T) = f_{SB_0}K_{RE}(\dot{\varepsilon},T)$. Therefore, the modified constitutive law comprising the behaviour even at different temperatures becomes, for the elastic and plastic parts respectively:

$$\sigma = E\left(\dot{\varepsilon},T\right)\varepsilon \qquad \text{for} \qquad \sigma<\sigma_y \tag{10a}$$

$$\sigma = \left[1-\frac{f_{SB}\left(\dot{\varepsilon},T\right)}{1+e^{a-b\varepsilon_p}}\right]\left(A+B\varepsilon_p^n\right)K_{RE}\left(\dot{\varepsilon},T\right) \tag{10b}$$

The calibration of material constitutive parameters has been performed by the minimisation of an RMS error function between the engineering experimental data and the analytical curves obtained by equation 10b (converted back into engineering values). It is worth noting that a more rigorous calibration would require an inverse FEM approach, due to the occurrence of deformation inhomogeneities. However, it will be shown that the analytical calibration is able to provide an acceptable accuracy. Furthermore, applying inverse FEM over such a large test campaign would require the iterative minimization of a global error function (which should be a weighted average of 16 RMS errors), comprising the risks of computational instabilities associated with strain or temperature concentrations. The goodness of this analytical calibration will be shown in the subsequent FEM validation.

The results of calibration are shown in Figure 8, where it is possible to observe an overall excellent agreement among the calculated and experimental engineering stress-strain curves. The material parameters are reported in Table 4. The average error in the calibration, i.e. the RMS deviation between experimental and numerical stress curves, is 5.06 MPa.

It is worth noting that the analytical stress calculation has been implemented following an incremental approach, where the stiffness of the stress-strain curve is computed at any time point. This approach coincides with the FEM implementation described in the next section and permits to account for the effective strain rate (which is not constant during the test) and temperature variations (due to self-heating). However, while FEM can account for eventual non-uniform distributions, the strain rate and temperature are considered uniformly distributed in the analytical model calibration.

Table 4 - Modified Nowak-Peçherski parameters for iPP

a	b	f_{SB_0}	B [MPa]	n
1.6706	12.6730	0.024	511.1	0.00515

The parameter A does not appear in Table 4 since it is implicitly defined by the other parameters. Indeed, being σ_0 a constant, from Equations (9) and (10b) it is inferred that the parameter A must vary with strain rate and temperature. At the Yield point, it results $\varepsilon_p = 0$ and the two equations must coincide, thus resulting:

$$A(\dot{\varepsilon},T) = \sigma_0 \Big/ \left(1 - \frac{f_{SB}(\dot{\varepsilon},T)}{1+e^{a-b\varepsilon_p}}\right) \tag{11}$$

In any case, substituting the parameter values of Table 4 into (11), A is found to be in the range 36.6-37.1 MPa for the investigated strain rate and temperature intervals.

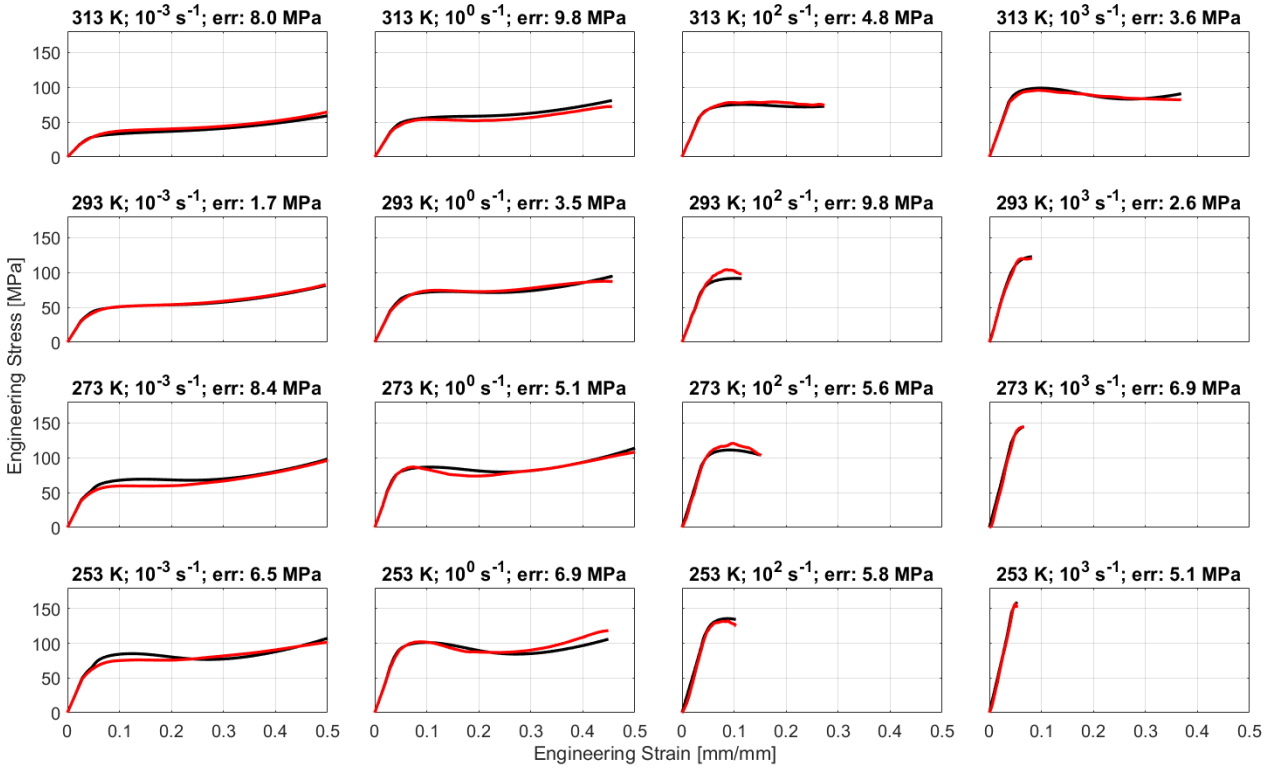

Figure 8 - Calibration results at different strain rates and temperatures (red curve: experimental, black curve: analytical). The test temperature, the strain rate and the RMS error (in MPa) are reported above each chart

Prediction of shear bands formation

As aforementioned, the first multiplicative term in the stress equations (8) and (10b) is responsible of the shape of the stress-strain curve at constant strain rate and temperature, and may describe the stress softening after the initial yielding or peak. In particular, the f_{SB} parameter that governs the amplitude of the stress drop is found to vary with strain rate and temperature as shown in Figure 9.

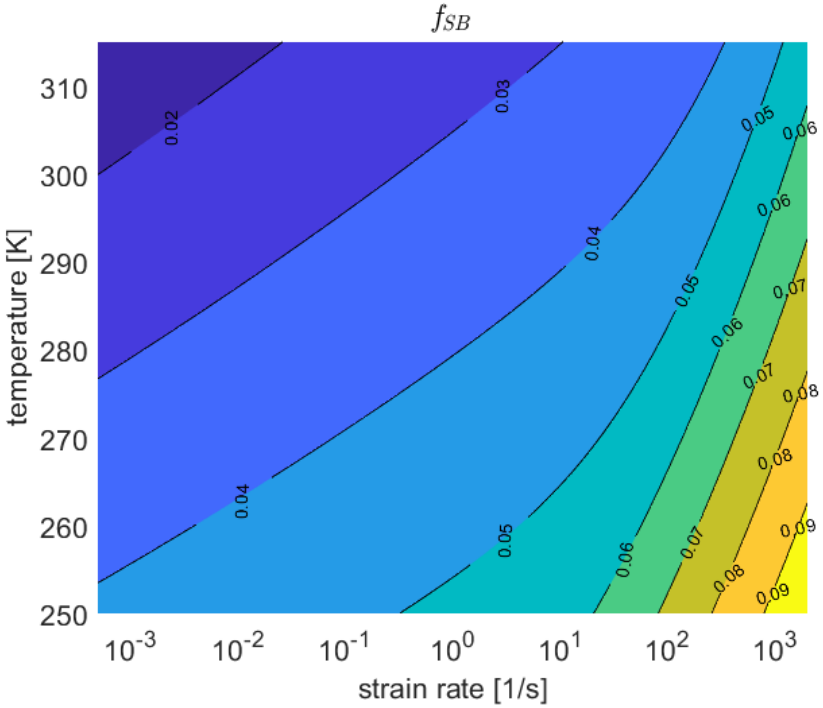

Figure 9 - Contour map of f_{SB} as a function of strain rate and temperature

It is noted that the f_{SB} term is small for lower strain rate and higher temperature; hence, it is likely to determine small deviation of the true stress-strain curve from the classic power law shape. On the other hand, f_{SB} increases at higher strain rate and/or lower temperature, so that the shape of true stress-strain may change significantly, showing a local peak after the yielding followed by a stress decrease. This behaviour of the true-stress strain curve can be considered as an instability that occurs internally in the material itself. While in tensile stress states the necking phenomenon occurs [30], in compression states the decrease of material strength determines a global instability in the form of a shear band. The onset of macroscopic shear bands is a global instability that derives precisely from this peculiar behaviour of the true stress-strain curve.

In addition, it should be recalled that the proposed model can predict the onset of macroscopic shear bands. In the simplifying hypothesis of constant volume and uniform deformation, as well known, the expression of the load as a function of true stress, true strain and initial cross-section A_0 holds:

$$P = \sigma(\varepsilon_p) A_0 e^{\varepsilon_p} \tag{12}$$

The derivative of the load with respect to the plastic deformation, normalized by A_0 becomes:

$$\frac{dP}{A_0 d\varepsilon_p} = H = \frac{d\sigma(\varepsilon_p)}{d\varepsilon_p} e^{\varepsilon_p} + e^{\varepsilon_p}\sigma(\varepsilon_p) \tag{13}$$

Basically, H represents a hardening function computed on the engineering stress. Substituting (10b) into (13), it is achieved:

$$H = e^{\varepsilon_p}\left[K_{RE}(\dot{\varepsilon},T)C + \sigma(\varepsilon_p)\right] \tag{14}$$

where C stands for the derivative of the first two terms in (10b):

$$C = -\frac{f_{SB} b e^{\left(a-b\varepsilon_p\right)}}{\left[1+e^{\left(a-b\varepsilon_p\right)}\right]^2}\left(A + B\varepsilon_p^n\right) + \left[1 - \frac{f_{SB}}{1+e^{\left(a-b\varepsilon_p\right)}}\right] Bn\varepsilon_p^{n-1} \tag{15}$$

The condition of global instability, associated with the onset of shear band, occurs if $dP/d\varepsilon_p \leq 0$ or, in other words, if $H \leq 0$. H depends on the strain rate and temperature and varies along with ε_p. Figure 10 shows the contour map of the minimum value of H computed at different strain rates and temperatures in the strain interval $0 < \varepsilon_p < 0.5$. The contour level $H = 0$ discriminates the strain rate-temperature field in two areas: in the yellow region, where $H > 0$, the load-deformation curve has always a positive slope and no shear bands are to be expected. On the contrary, in the regions below the contour level $H = 0$, the load-deformation curves do have a negative slope, and shear band instability is likely to occur after a local peak.

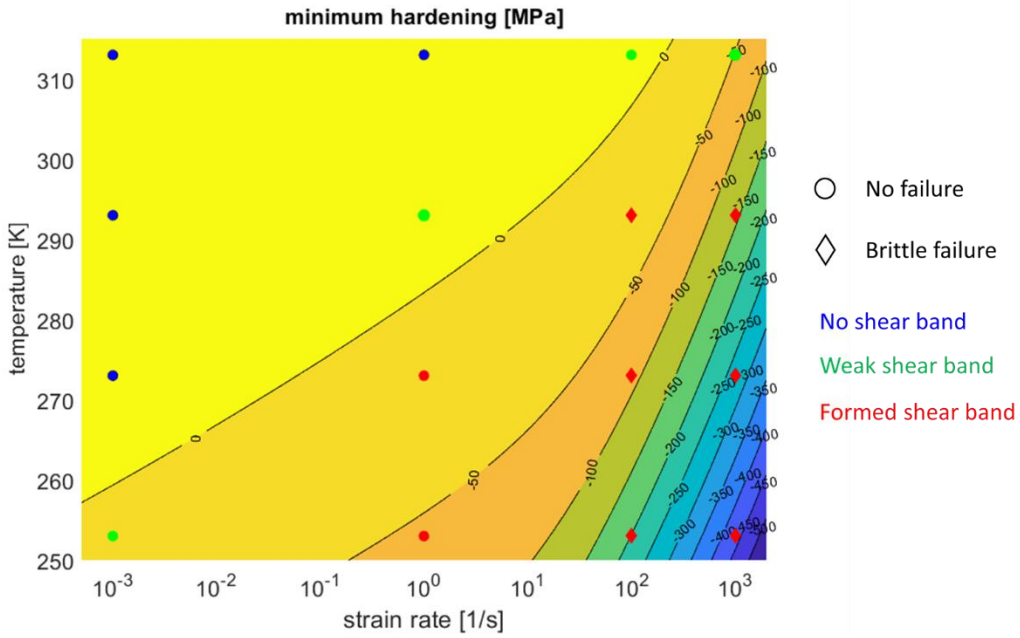

Figure 10 - Contour map of the minimum hardening function given by (14) computed in the strain interval 0-0.5. The markers denote the experimental observation

FEM Analyses

Finite element simulations of the compression tests have been carried out to compare experimental and numerical results after the analytical calibration of the constitutive model. A similar approach can be found in Deng et al. [57] for PMMA at strain rates from 10^{-4} up to 10^{-2} 1/s. Thus, the FE model was realized in Abaqus®/Explicit software, using the Lagrangian solver. The model, meshed with bidimensional axisymmetric elements (CAX4R), is shown in Figure 11. Displacement boundary conditions at each side (specimen supports or input/output bars) have been set equal to those measured during real tests. The input and output bar interfaces at the specimen ends were modelled as rigid. The contact and friction algorithms used in the simulations were surface-to-surface contact, with "hard" normal behaviour and frictional tangential behaviour, implemented with the penalty method . A low friction coefficient (0.04) has been set at the specimen interfaces, since lubrication was used in the experiments.

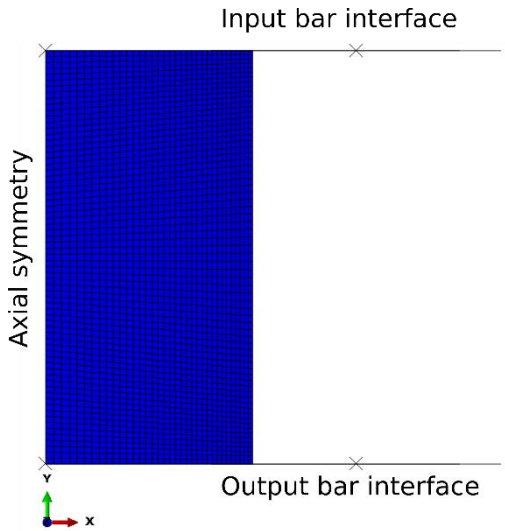

Figure 11 - Axisymmetric FE model of the specimen

The modified Nowak-Peçherski constitutive model described in the previous section has been implemented by means of a user-defined subroutine (*Vumat*). The coefficients adopted are those reported in Table 4. Young modulus and Yield stress dependences on strain rate and temperature have been considered in accordance with the calibrated Ree-Eyring models, using the coefficients given in Table 3. The standard von Mises equivalent stress and the isotropic hardening were used as yield criterion and plastic flow rule, respectively, in the *Vumat* subroutine. Details about the implementation of the user-defined material within the framework of large strain are given in Appendix 2.

Stress and strain behaviour

In Figure 12, the FE results are shown together with the experimental ones, in terms of engineering stress-strain curves. The red curves are the experimental ones, while the blue curves are the numerical ones. It can be noted that the numerical simulations at 10^2 and 10^3 s^{-1} reached deformations that are higher than those experienced by the real samples (represented in blue dashed line); nevertheless, when the load-bearing capability decreases too much, the simulations suffer from convergence problem and stop. However, a very good matching can be observed in general, validating the implemented procedure.

According to Figure 12, the FEM curves show that the load is monotonically increasing for tests conducted at strain rate from 10^{-3} to 10^0 s^{-1}, at temperature from 293K to 313K. The samples tested

in these conditions were deformed uniformly, exception made for a limited barrelling, up to the maximum load.

The conditions of 10^{-3} s^{-1} strain rate at 293K and 10^{2} s^{-1} at 313K are close to the frontier $H = 0$, as their load-displacement curve have a nearly flat portion. The samples tested in these conditions showed a slightly inhomogeneous deformation, meaning that a sort of weak shear band started, but did not develop completely.

All other combinations of strain rate and temperature that are characterized by $H < 0$ show a relevant decrement of the load-bearing capacity computed by FEM. This is the case of all the tests at 10^{2} and 10^{3} s^{-1}, and all the tests at 273 K, which were indeed characterized by clear shear bands formation, as shown in Figure 1.

It is worth reminding that the proposed model can predict the shear bands to form even in absence of friction, and nearly identical load-displacement curves have been obtained with different friction coefficients varying from 0.0 to 0.04 and 0.08. This is a good point, since it means that the shear bands initiation occurs due to the material behaviour, even in uniaxial stress state, and does not need necessarily an external trigger, such as frictional shear stresses. However, it must be admitted that in real tests friction may play a role and can favour the shear bands initiation. Indeed, some points falling in the region $H > 0$ of Figure 10 showed a certain inhomogeneous deformation due to limited shear band formation.

Figure 13 shows the contour map of von Mises stress computed by the FEM at the instant of maximum strain experimentally measured. It is seen that in the three upper-left pictures the stress distribution is quite uniform, despite some barrelling occurred; other simulations show less uniform deformation and stress distribution. The tests characterized by brittle failure of the samples, i.e. those at strain rate 10^{2}-10^{3} s^{-1} and T<313K, show clear shear bands at the final instant of the test, after with specimens separate in pieces.

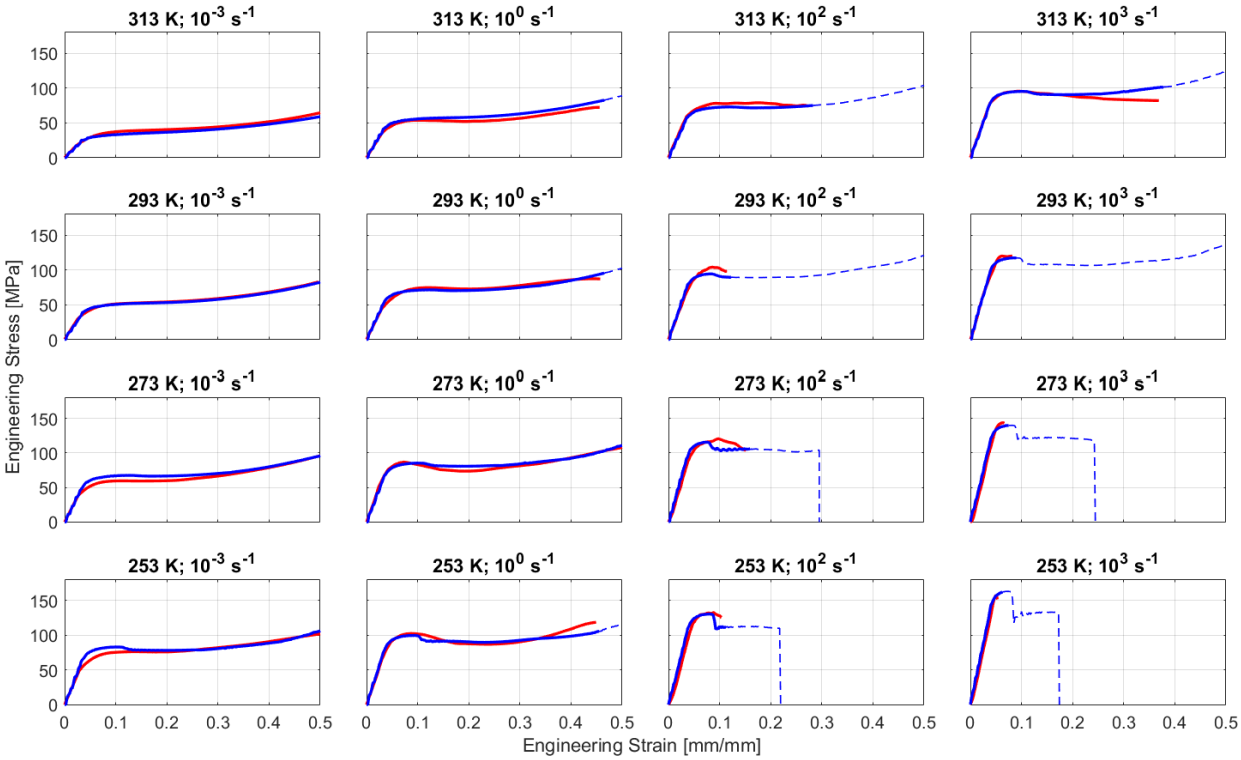

Figure 12 - Comparison between experimental (red) and numerical (blue) results

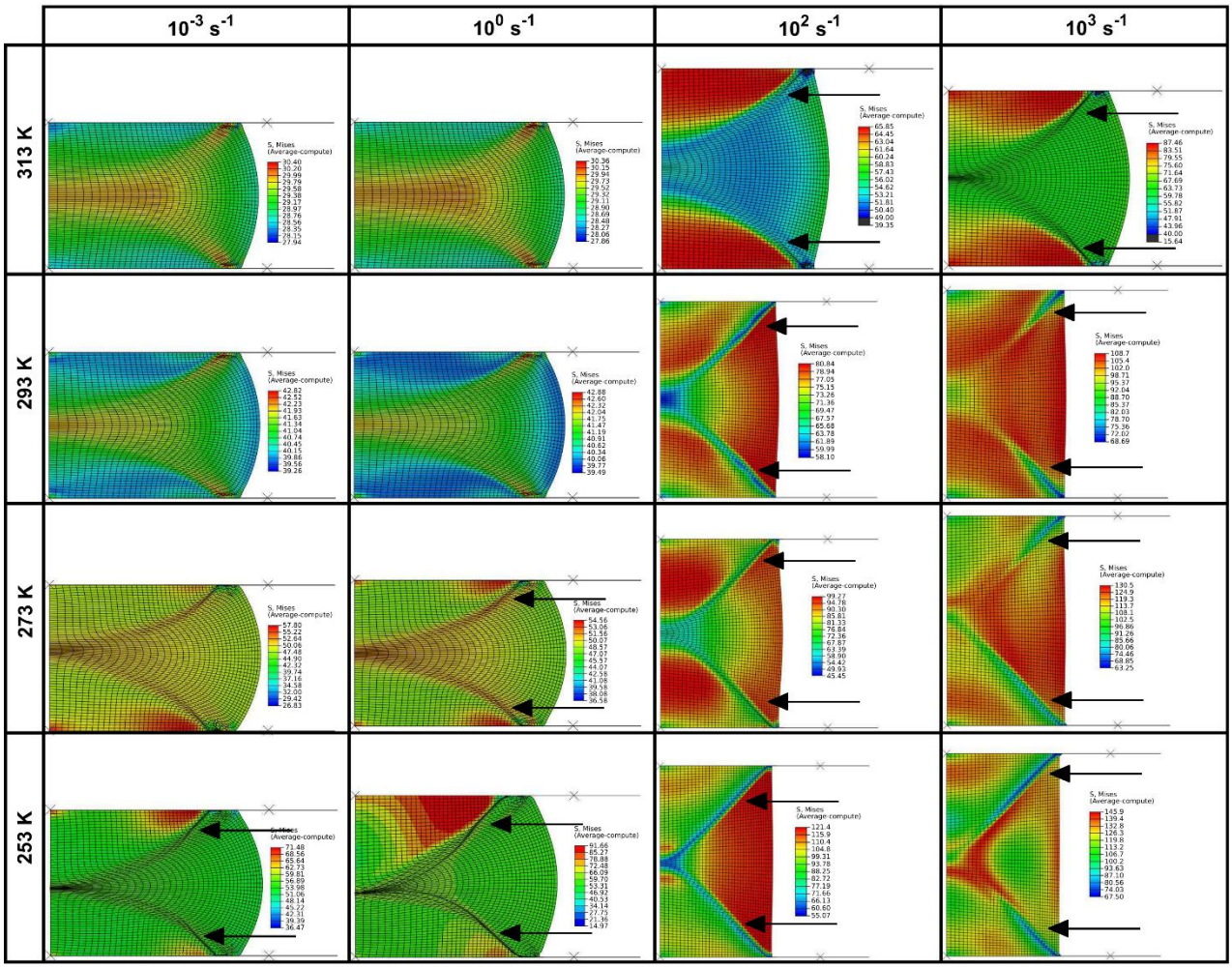

Figure 13 - Von Mises stress contour maps computed by at the maximum experimental strain value for each test. The black arrows highlight the regions characterized by the formation of shear bands (see also the strain contour maps in Figure 16).

Self-heating effect

As aforementioned, only the tests at 10^{-3} s^{-1} can be considered isothermal, whereas tests at strain rate 10^{0} s^{-1} or higher are to be considered adiabatic and self-heating in the sample takes place due to plastic work. Moreover, since the deformation is uniform only for a few tests, all other conditions are likely to induce largely non-uniform temperature distribution.

The entire plastic work has been considered to be converted into heat; then, the current temperature can be computed by $T = T_0 + \int \sigma d\varepsilon \big/ \rho C_p$, where T_0 is the initial temperature, and ρ and C_p are the material density (908 kg·m^{-3}) and specific heat (1800 J·kg^{-1}·K^{-1}) respectively. The temperature distribution maps obtained at the last converged step by FEM analyses are shown in Figure 14.

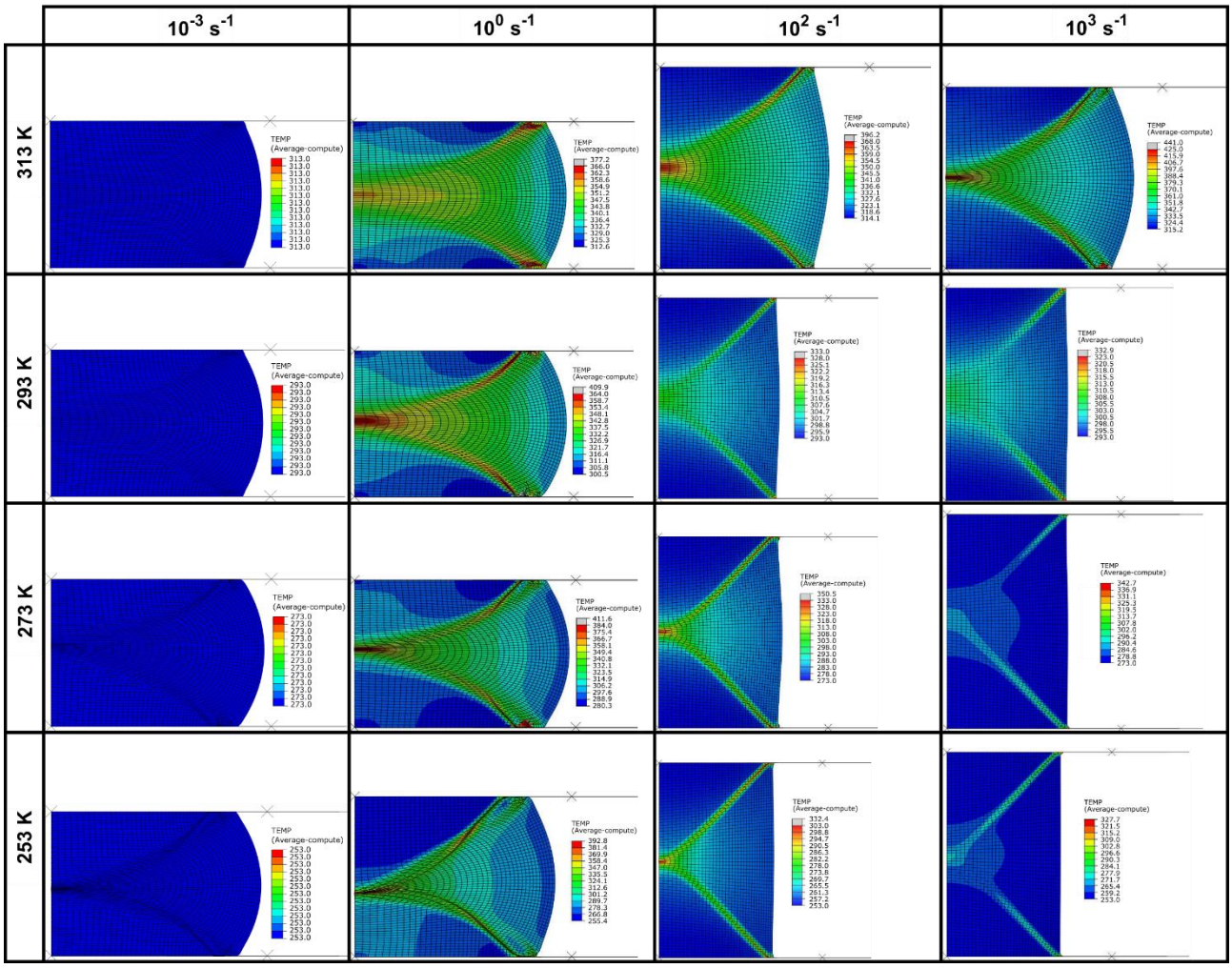

Figure 14 - Temperature contour maps

It is noted that the temperature increases significantly in the zones where the shear strain localizes; however, the increment in the average temperature of the samples is much more limited. Figure 15 shows the temperature evolution computed by FEM for all tests as a function of engineering strain. The solid lines describe the temperature of the material point that will exhibit the maximum shear strain at the last significant instant of the test; the dashed lines represent the temperature averaged over all section nodes.

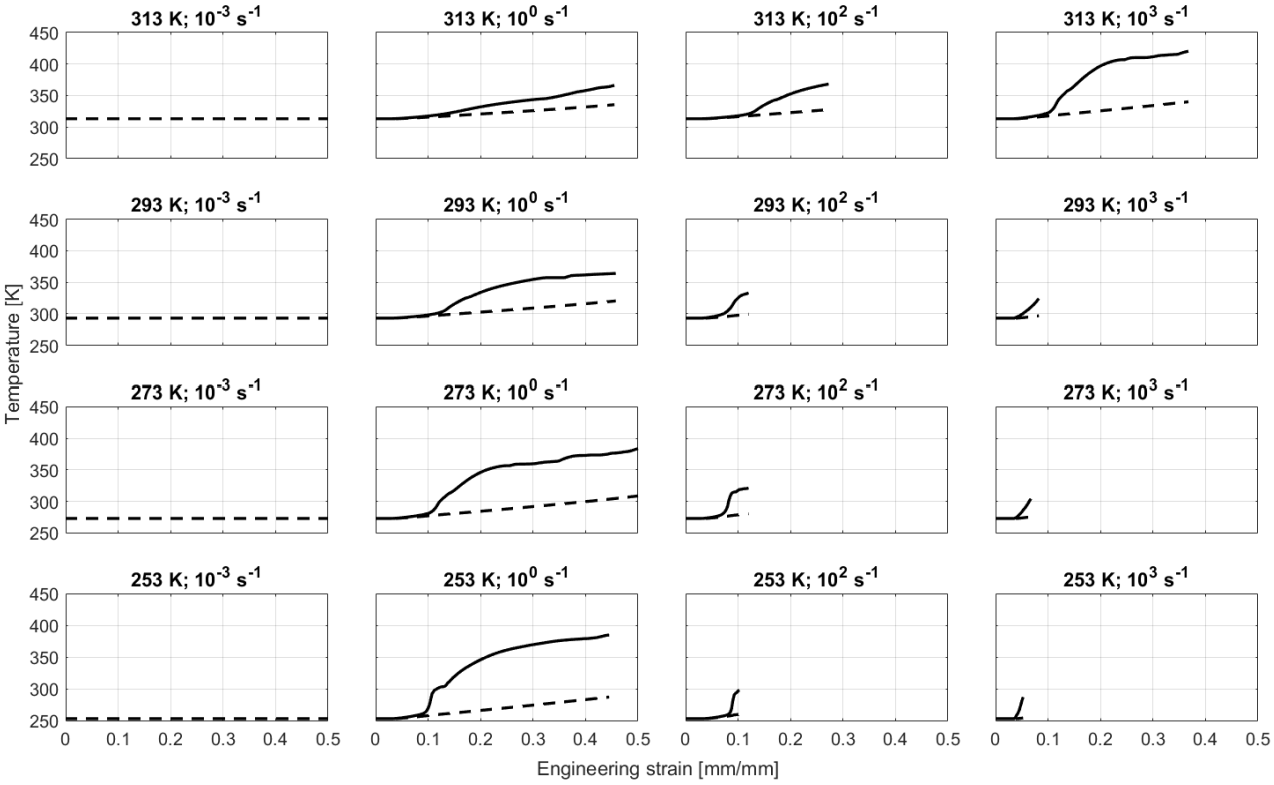

Figure 15 - Temperature evolution. Dashed line: section average, solid line: point of maximum shear

In the tests that achieved 0.5 of engineering strain, the maximum temperature rise was about 100K or even more in some cases; the tests at high strain rate characterized by lower engineering strain at the final instant before failure showed lower temperature increment, in the order of 50-70 degrees in the regions of maximum shear strain. In all cases, the average temperature increase due to the conversion of plastic work into heat is much lower.

Shear strain to failure analysis

The shear bands formation and a quantitative evaluation of shear strain are better understood by observing the contour maps of logarithmic shear strain (LE12) shown in Figure 16. The higher values of shear strain originate from the most external contact region of the sample with the rigid surfaces. However, whereas the maximum shear strain distributes over a certain area for the samples characterized by nearly uniform deformation, the maximum shear strain localizes in narrow bands, clearly distinguished by those red and blue "tongues" in all the tests at 253K and all tests at high strain rate. Moreover, the tests at 10^2-10^3 s^{-1} at temperature T≤293K experienced a brittle failure. The failure initiates, as observed in videos recorded by the high-speed camera, with shear bands

formation; then, the combinations of low temperature and/or high strain rate reduces the strain to failure of the material.

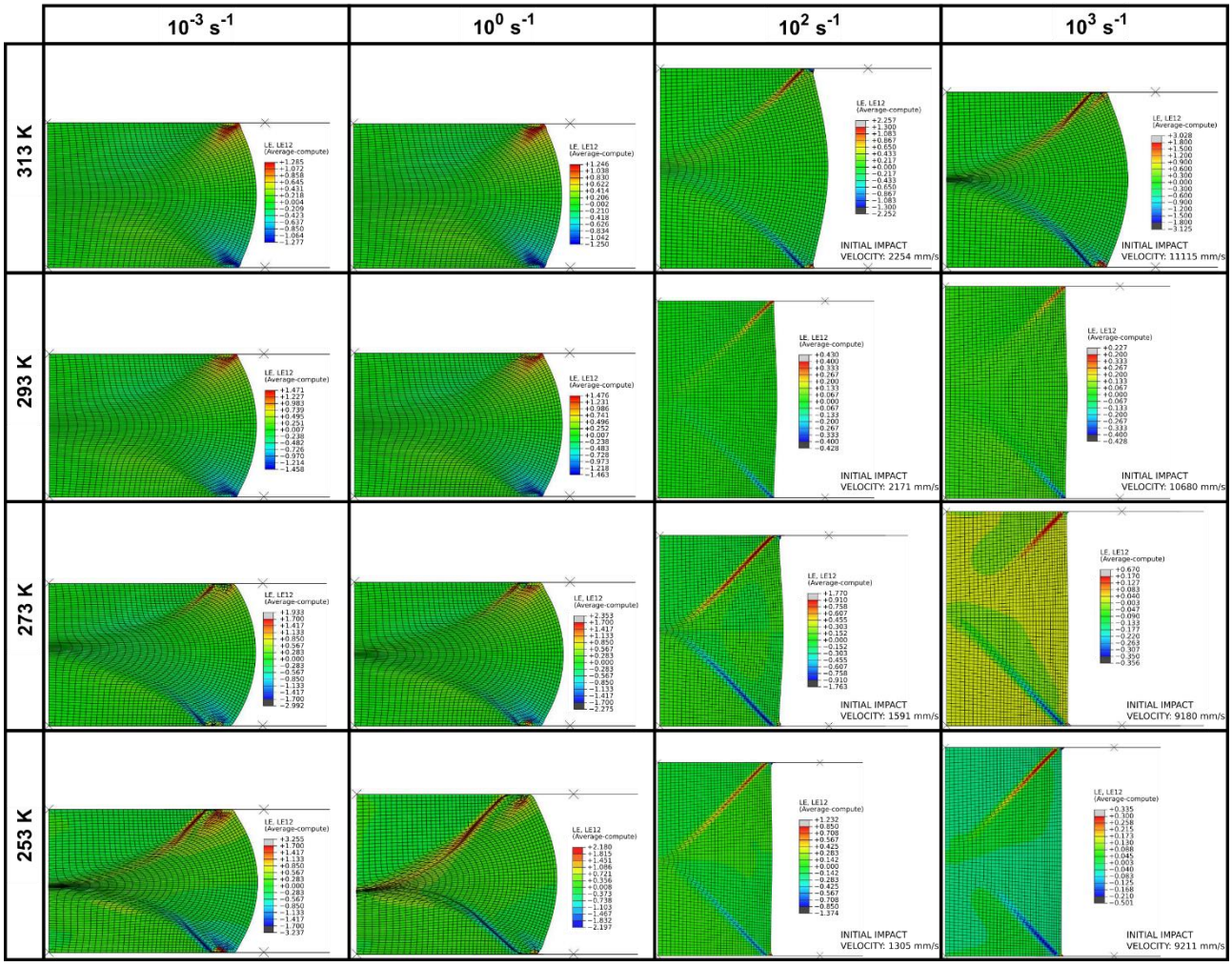

Figure 16 - Shear strain maps showing adiabatic shear bands under dynamic conditions

CONCLUSIONS

This study shows the development of a constitutive model capable of describing the compressive behaviour of polymers showing the shear bands instability. This phenomenon has been observed on an isotactic Polypropylene, tested in a wide range of strain rates and temperatures.

The model is inspired by the Nowak-Peçherski law for describing the non-linear relation between stress and strain. Since mechanical properties of Polypropylene show a significant dependence on strain rate and temperature, their effects have been introduced by using a factor inspired by the Ree-Eyring law. Such a factor affects both the material strength and the shape of the stress-strain curve. Consequently, the model can be used to predict the occurrence of shear bands for specific values of strain rate and temperature combinations.

The constitutive parameters have been evaluated by an analytical calibration performed on experimental data obtained in a recent work. The proposed constitutive model has been validated numerically, implementing it within a commercial FEM code by means of a user-defined subroutine. The results of the simulations are in excellent agreement with the experimental measurements; the numerical model captured very well not only the global stress-strain behaviour but also the shear bands formation (that govern the failure mode) observed in real experiments.

APPENDIX 1 – SHB technique

The dynamic tests have been carried out by a Split Hopkinson Bar. The experiments have been also recorded with a high-speed camera, model Photron® SA4 at 10^5 fps, in order to investigate the behaviour of the specimen at high velocities. SHB is the most commonly used apparatus for dynamic testing on metals and engineering materials, from tension to compression and torsion. Only the basics of the Hopkinson Bar method, which is relevant for understanding the present work, is reported here; more details on this technique can be found in [32].

The Hopkinson bar method exploits the elastic pressure waves that travel in straight long bars with the sample that is sandwiched between two bars. Typically, the pressure wave is generated by the impact that occurs between a "striker bar" and an "input bar"; alternatively, the stress wave can be generated by preloading and fast releasing a portion of the input bar. Then, the wave propagates at sound speed along the input bar until it reaches the sample. At this point, the latter is dynamically loaded, while the pressure waves are partially reflected back in the input bar and partially transmitted in the output one (Figure A1).

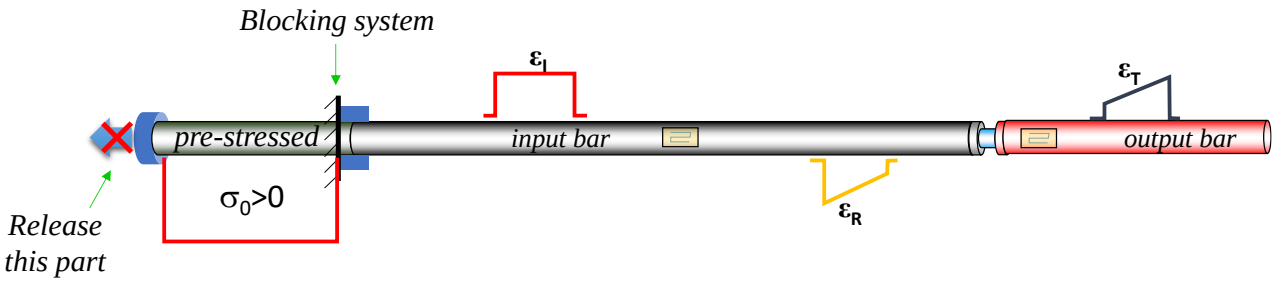

Figure A1 - Scheme of a direct SHB

By measuring the strain amplitudes of the waves travelling along the bars (e.g. by means of strain gauges), it is possible to evaluate the engineering strain rate, strain and stress histories experienced by specimen material with the following equations:

$$\dot{\varepsilon}(t) = -\frac{2C_0}{L_S}\varepsilon_R(t) \tag{A1}$$

$$\varepsilon(t) = -\frac{2C_0}{L_s}\int_0^t \varepsilon_R(\tau)\cdot d\tau \tag{A2}$$

$$\sigma(t) = \frac{A_b \cdot E_b}{A_s} \varepsilon_T(t) \tag{A3}$$

where L_s and A_s represent the specimen length and cross-section area, A_b, E_b and C_0 represent the cross-section, Young modulus and material sound speed of the bars.

Whereas the tested specimen deforms significantly up to large strain or even failure, the bars are made to remain well below their elastic limit. The pre-stressed, input and output bars are 3.0, 7.5 and 4.0 m long, respectively; the diameter is 18 mm for all bars. Strain measurements are performed by strain gauges glued at half of the input bar and 0.10 m away from the specimen in the output bar. The full Wheatstone bridge configuration was used for all strain gauges. A NI® 6120 acquisition card at the sampling frequency of 1 MHz acquires the voltage signals coming from the two Wheatstone bridges simultaneously. A picture of the SHB with the sample is shown in Figure A2.

The temperature is set by means of Vortec® compressed air guns adopting the following method; the sample is mounted between the bars and closed inside an external casing to form a small chamber, while adjustable jets of hot or cold air are directed inside the casing for a sufficient time (i.e. approximately 15 minutes) to reach a stable temperature. The temperature is evaluated continuously by means of 2 thermocouples glued to opposite sides of the lateral surface of the specimen as shown in Figure A2c (reproduced from [31]), while the casing is removed a few seconds before the test.

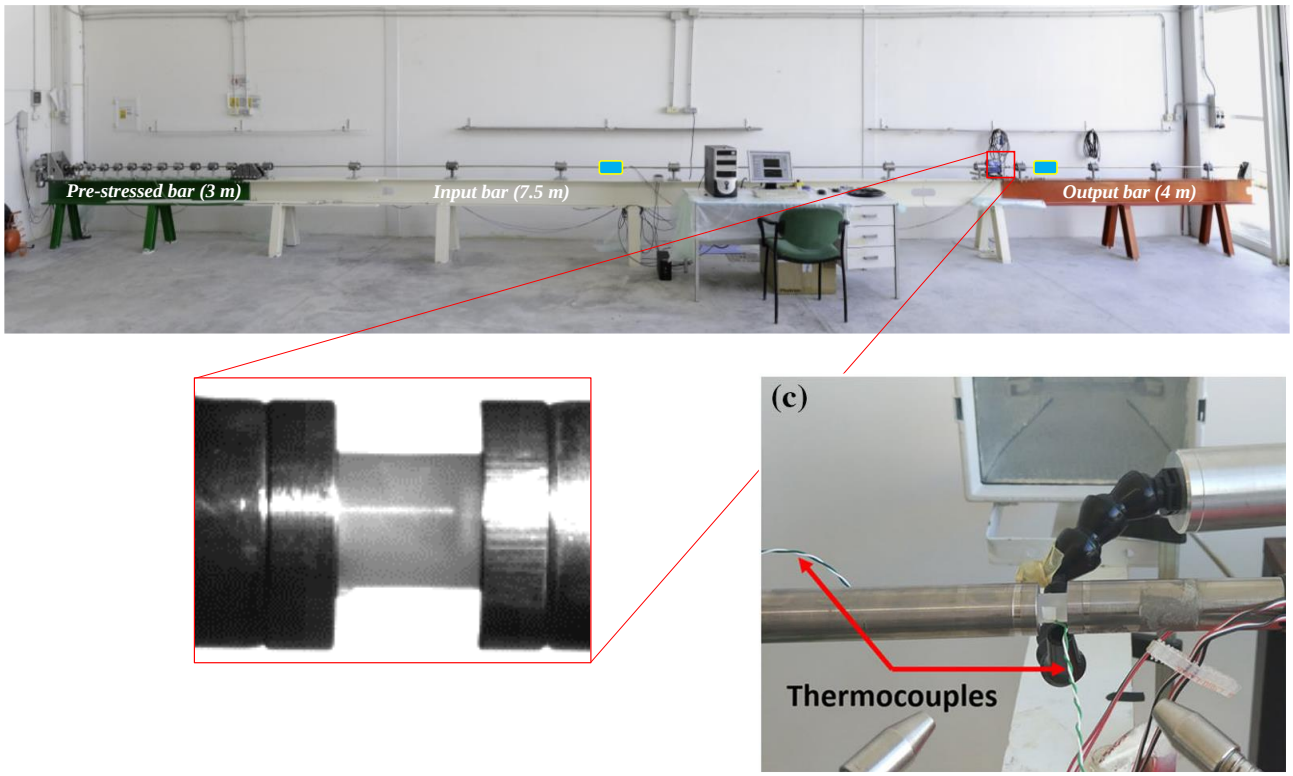

Figure A2 - Tension-Compression Split Hopkinson Bar with sample

APPENDIX 2 – Vumat implementation

The developed user-defined material has been implemented in a routine written in Fortran programming language (Vumat). At each time increment, the routine receives from Abaqus the deformation gradient tensor and the strain increments as input, computes the stress rate according to Green-Naghdi formulation in corotational framework, and returns to Abaqus the updated Cauchy stress. The forward Euler integration is used to integrate the constitutive rate equation, while the constitutive equations (10a) and (10b) are used to describe the equivalent stress-strain behaviour of the material.

Governing equations:

In elasticity, the Cauchy stress components can be written as follows:

$$\sigma_{ij} = 2\mu\varepsilon_{ij}^{el} + \lambda\delta_{ij}\sum_{k=1}^{3}\varepsilon_{kk}^{el} \tag{A4}$$

In a Green-Naghdi corotational framework, the stress increments are readily:

$$\Delta\sigma_{ij} = 2\mu\Delta\varepsilon_{ij}^{el} + \lambda\delta_{ij}\sum_{k=1}^{3}\Delta\varepsilon_{kk}^{el} \tag{A5}$$

where μ and λ are the classic Lamè elastic constants, δ_{ij} is the Kronecker operator, and $\Delta\varepsilon_{ij}^{el}$ are the logarithmic Hencky strain increments. The use of the logarithmic strain is often exploited for the numerical integration of constitutive equations in incremental form for large deformation plasticity problems [58, 59], and thus adopted by Abaqus as input for the stress reconstruction.

Analogously, the strain and strain rate are additively decomposed into an elastic (*e*) and plastic (*p*) part:

$$\dot{\varepsilon}_{ij} = \dot{\varepsilon}_{ij}^{e} + \dot{\varepsilon}_{ij}^{p} \tag{A6}$$

$$\varepsilon_{ij} = \varepsilon_{ij}^{e} + \varepsilon_{ij}^{p} \tag{A7}$$

When the elastic limit is exceeded, the von Mises Yield criterion is used to compute the equivalent stress σ_y as a function of equivalent plastic strain $\bar{\varepsilon}^p$; the yield function is given by:

$$\sigma_y\left(\bar{\varepsilon}^p\right) = q = \sqrt{\frac{3}{2}S_{ij}S_{ij}} \tag{A8}$$

where S_{ij} are the deviatoric stresses

$$S_{ij} = \sigma_{ij} - \frac{1}{3}\delta_{ij}\sum_{k=1}^{3}\sigma_{kk} \tag{A9}$$

Assuming that the principal directions of stress and plastic strain coincide, the Isotropic Hardening flow rule is used to compute the evolution laws of plastic strains components. The flow rule is:

$$\dot{\varepsilon}_{ij}^{p} = \left(\frac{3S_{ij}}{2\sigma_y}\right)\dot{\bar{\varepsilon}}^{p} \tag{A10}$$

Equations (A7) and (A8) define the material behaviour. At any increment, the occurrence of plastic flow is determined by evaluating q based on purely elastic response; these equations are to be integrated by applying the forward Euler method to the flow rule (A10).

Implementation scheme

In the Vumat code, the integration of the Cauchy stress has to be performed explicitly at each time increment from instant $t-\Delta t$ to instant t:

$$\sigma_{ij}(t) = \sigma_{ij}(t-\Delta t) + \Delta\sigma_{ij} \tag{A11}$$

The elastic predictor method is used to determine the occurrence of yielding; in fact, the deviatoric stress components are:

$$S'_{ij} = S'_{ij}(t-\Delta t) + 2\mu\Delta e_{ij} \tag{A12}$$

where Δe_{ij} are the deviatoric strain increments, and the equivalent stress predictor is

$$\bar{\sigma}' = \sqrt{\frac{3}{2}S'_{ij}S'_{ij}} \tag{A13}$$

When the elastic predictor is lower than the yield stress, equations (A5) and (A11) can be used to update the Cauchy stress tensor at the end of the time increment. On the other hand, plastic flow occurs when the elastic predictor is larger than the current yield stress σ_y; using the Newton method, the increment of equivalent plastic strain in the time step is obtained by [60]:

$$\Delta\bar{\varepsilon}^{p} = \frac{\bar{\sigma}' - \sigma_y}{3\mu + K} \tag{A14}$$

where $K = d\sigma_y / d\bar{\varepsilon}^p$ is the hardening rate, i.e. the derivative of the equation (10):

$$K = K_{RE}\left(\dot{\bar{\varepsilon}}^p, T\right)\left\{-\left[A + B\left(\bar{\varepsilon}^p\right)^n\right]\frac{f_{SB}(\dot{\bar{\varepsilon}}^p, T)be^{\left(a-b\bar{\varepsilon}^p\right)}}{\left[1+e^{\left(a-b\bar{\varepsilon}^p\right)}\right]^2} + Bn\left(\bar{\varepsilon}^p\right)^{n-1}\left[1-\frac{f_{SB}(\dot{\bar{\varepsilon}}^p, T)}{1+e^{\left(a-b\bar{\varepsilon}^p\right)}}\right]\right\} \quad \text{(A15)}$$

The current yield stress can now be updated:

$$\sigma_y(t) = \sigma_y(t-\Delta t) + K\Delta\bar{\varepsilon}^p \quad \text{(A16)}$$

Notice that *K* accounts for the equivalent plastic strain rate $\dot{\bar{\varepsilon}}^p$ (i.e. $\Delta\bar{\varepsilon}^p/\Delta t$) and for the temperature *T* that have been computed in the previous integration step. Integration of the plastic work gives the temperature at the end of the current step:

$$T(t) = T(t-\Delta t) + \frac{1}{2}\left[\sigma_y(t-\Delta t) + \sigma_y(t)\right]\frac{\Delta\bar{\varepsilon}^p}{\rho C_p} \quad \text{(A17)}$$

The sought Cauchy stress tensor can be computed:

$$\sigma_{ij} = f_{ij}\sigma_y + \frac{1}{3}\delta_{ij}\sum_{K=1}^{2}\sigma'_{kk} \quad \text{(A18)}$$

with $f_{ij} = S'_{ij}/\bar{\sigma}'$. In addition, the components of plastic strain can be updated according to equation (A10):

$$\varepsilon_{ij}^p(t) = \varepsilon_{ij}^p(t-\Delta t) + \frac{3}{2}f_{ij}\Delta\bar{\varepsilon}^p \quad \text{(A19)}$$

REFERENCES

1. Klompen E (Edwin) (2005) Mechanical properties of solid polymers:constitutive modelling of long and short term behaviour. Eindhoven University of Technology

2. Bajsić EG, Šmit I, Leskovac M (2006) Blends of thermoplastic polyurethane and polypropylene. I. Mechanical and phase behavior. J Appl Polym Sci 104:. https://doi.org/10.1002/app.26222

3. Dixit M, Shaktawat V, Sharma K, et al (2008) Mechanical Characterization of Polymethyl Methacrylate and Polycarbonate Blends. In: AIP Conference Proceedings. pp 311–316

4. Zaim A, Ouled-chikh E, Bouchouicha B (2018) Thermo-Mechanical Characterization of a Thermoplastic Copolyetherester (TPC): Experimental Investigation. Fibers Polym 19:734–741. https://doi.org/10.1007/s12221-018-7455-1

5. Sahputra IH, Echtermeyer AT (2013) Effects of temperature and strain rate on the deformation of amorphous polyethylene: a comparison between molecular dynamics simulations and experimental results. Model Simul Mater Sci Eng 21:. https://doi.org/10.1088/0965-0393/21/6/065016

6. Richeton J, Ahzi S, Vecchio KS, et al (2006) Influence of temperature and strain rate on the mechanical behavior of three amorphous polymers: Characterization and modeling of the compressive yield stress. Int J Solids Struct 43:2318–2335. https://doi.org/10.1016/j.ijsolstr.2005.06.040

7. Cao K, Wang Y, Wang Y (2014) Experimental investigation and modeling of the tension behavior of polycarbonate with temperature effects from low to high strain rates. Int J Solids Struct 51:2539–2548. https://doi.org/10.1016/j.ijsolstr.2014.03.026

8. Siviour CR, Walley SM, Proud WG, Field JE (2005) The high strain rate compressive behaviour of polycarbonate and polyvinylidene difluoride. Polymer (Guildf) 46:12546–12555. https://doi.org/10.1016/j.polymer.2005.10.109

9. Dar UA, Zhang W, Xu Y, Wang J (2014) Thermal and strain rate sensitive compressive behavior of polycarbonate polymer - experimental and constitutive analysis. J Polym Res 21:. https://doi.org/10.1007/s10965-014-0519-z

10. Al-Juaid AA, Othman R (2016) Modeling of the Strain Rate Dependency of Polycarbonate's Yield Stress: Evaluation of Four Constitutive Equations. J Eng 1–9.

https://doi.org/10.1155/2016/6315421

11. El-Qoubaa Z, Othman R (2015) Tensile Behavior of Polyetheretherketone over a Wide Range of Strain Rates. Int J Polym Sci 2015:1–9. https://doi.org/10.1155/2015/275937

12. Gómez-del Río T, Rodríguez J (2012) Compression yielding of epoxy: Strain rate and temperature effect. Mater Des 35:369–373. https://doi.org/10.1016/j.matdes.2011.09.034

13. Tamrakar S, Ganesh R, Sockalingam S, et al (2018) Experimental Investigation of Strain Rate and Temperature Dependent Response of an Epoxy Resin Undergoing Large Deformation. J Dyn Behav Mater 4:114–128. https://doi.org/10.1007/s40870-018-0144-8

14. Brinson HF, Brinson LC (2008) Polymer engineering science and viscoelasticity, 2nd ed. Springer, Boston, MA, New York

15. Li Z, Lambros J (2001) Strain rate effects on the thermomechanical behavior of polymers. Int J Solids Struct 38:3549–3562. https://doi.org/10.1016/s0020-7683(00)00223-7

16. Plaseied A, Fatemi A (2008) Strain Rate and Temperature Effects on Tensile Properties and Their Representation in Deformation Modeling of Vinyl Ester Polymer. Int J Polym Mater Polym Biomater 57:463–479. https://doi.org/10.1080/00914030701729677

17. Brown EN, Rae PJ, Orler EB (2006) The influence of temperature and strain rate on the constitutive and damage responses of polychlorotrifluoroethylene (PCTFE, Kel-F 81). Polymer (Guildf) 47:7506–7518. https://doi.org/10.1016/j.polymer.2006.08.032

18. Newmann L V., Williams JG (1978) The impact behavior of ABS over a range of temperatures. Polym Eng Sci 18:893–899. https://doi.org/10.1002/pen.760181112

19. Gaymans RJ, Hamberg MJJ, Inberg JPF (2000) The brittle-ductile transition temperature of polycarbonate as a function of test speed. Polym Eng Sci 40:256–262. https://doi.org/10.1002/pen.11158

20. Kitao K (1997) A study of brittle-ductile transition in polyethylene. Polym Eng Sci 37:777–788. https://doi.org/10.1002/pen.11721

21. Friedrich K (1983) Crazes and shear bands in semi-crystalline thermoplastics. In: Kausch HH (ed) Crazing in Polymers. Springer Berlin Heidelberg, pp 225–274

22. Bowden PB, Raha S (1970) The formation of micro shear bands in polystyrene and polymethylmethacrylate. Philos Mag A J Theor Exp Appl Phys 22:463–482.

https://doi.org/10.1080/14786437008225837

23. Argon AS, Andrews RD, Godrick JA, Whitney W (1968) Plastic Deformation Bands in Glassy Polystyrene. J Appl Phys 39:1899–1906. https://doi.org/10.1063/1.1656448

24. Swallowe GM (1999) Mechanical Properties and Testing of Polymers. An A–Z Reference. Springer Netherlands

25. MEDYANIK S, LIU W, LI S (2007) On criteria for dynamic adiabatic shear band propagation. J Mech Phys Solids 55:1439–1461. https://doi.org/10.1016/j.jmps.2006.12.006

26. Rittel D (2009) A different viewpoint on adiabatic shear localization. J Phys D Appl Phys 42:. https://doi.org/10.1088/0022-3727/42/21/214009

27. Fleck NA (1999) Adiabatic Shear Instability: Theory. In: Swallowe GM (ed) Mechanical Properties and Testing of Polymers: An A--Z Reference. Springer Netherlands, pp 15–19

28. Wright TW (1990) Approximate analysis for the formation of adiabatic shear bands. J Mech Phys Solids 38:515–530. https://doi.org/10.1016/0022-5096(90)90012-s

29. Dodd B, Bai Y (2012) Adiabatic Shear Localization: Frontiers and Advances. Elsevier Science

30. Farotti E, Natalini M (2018) Injection molding. Influence of process parameters on mechanical properties of polypropylene polymer. A first study. Procedia Struct Integr 8:256–264. https://doi.org/10.1016/j.prostr.2017.12.027

31. Farotti E, Mancini E, Bellezze T, Sasso M (2019) Investigation of the Effects of Mold Temperature, Test Temperature and Strain Rate on Mechanical Behaviour of Polypropylene. J Dyn Behav Mater 5:344–360. https://doi.org/10.1007/s40870-019-00218-7

32. Mancini E, Sasso M, Rossi M, et al (2015) Design of an Innovative System for Wave Generation in Direct Tension--Compression Split Hopkinson Bar. J Dyn Behav Mater 1:201–213. https://doi.org/10.1007/s40870-015-0019-1

33. Mirone G, Corallo D, Barbagallo R (2016) Interaction of strain rate and necking on the stress-strain response of uniaxial tension tests by Hopkinson bar. Procedia Struct Integr 2:974–985. https://doi.org/10.1016/j.prostr.2016.06.125

34. Cadoni E, Forni D, Gieleta R, Kruszka L (2018) Tensile and compressive behaviour of S355 mild steel in a wide range of strain rates. Eur Phys J Spec Top 43:29–43.

https://doi.org/10.1140/epjst/e2018-00113-4

35. Liao Z, Yao X, Zhang L, et al (2019) Temperature and strain rate dependent large tensile deformation and tensile. International Journal of Impact Engineering 129:152–167. https://doi.org/10.1016/j.ijimpeng.2019.03.005

36. van Ekeren PJ, Carton EP. Polyurethanes for potential use in transparent armour investigated using DSC and DMA. J Therm Anal Calorim 2011;105(2):591–8. https://doi.org/10.1007/s10973-011-1665-8.

37. Ree T, Eyring H (1955) Theory of Non-Newtonian Flow. I. Solid Plastic System. J Appl Phys 26:793–800. https://doi.org/10.1063/1.1722098

38. Roetling J. (1965) Yield stress behaviour of poly(ethyl methacrylate) in the glass transition region. Polymer (Guildf) 6:615–619. https://doi.org/10.1016/0032-3861(65)90056-x

39. Roetling JA (1965) Yield stress behaviour of polymethylmethacrylate. Polymer (Guildf) 6:311–317. https://doi.org/10.1016/0032-3861(65)90081-9

40. Bauwens-Crowet C, Bauwens JC, Homès G (1969) Tensile yield-stress behavior of glassy polymers. J Polym Sci Part A-2 Polym Phys 7:735–742. https://doi.org/10.1002/pol.1969.160070411

41. Eyring H (1936) Viscosity, Plasticity, and Diffusion as Examples of Absolute Reaction Rates. J Chem Phys 4:283–291. https://doi.org/10.1063/1.1749836

42. Li JX, Cheung WL (1998) On the deformation mechanisms of β-polypropylene: 1. Effect of necking on β-phase PP crystals. Polymer (Guildf) 39:6935–6940. https://doi.org/10.1016/s0032-3861(98)00144-x

43. Porzucek K, Coulon G, Lefebvre JM, Escaig B (1989) Plastic flow of polypropylene (PP) and a PP-based blend. J Mater Sci 24:2533–2540. https://doi.org/10.1007/bf01174524

44. Gao R, Kuriyagawa M, Nitta K-H, et al (2015) Structural Interpretation of Eyring Activation Parameters for Tensile Yielding Behavior of Isotactic Polypropylene Solids. J Macromol Sci Part B 54:1196–1210. https://doi.org/10.1080/00222348.2015.1079088

45. Mancini E, Farotti E, Paoletti C, Sasso M (2019) Shear bands formation in different engineering materials subjected to dynamic compression. In: Proceedings of the 22nd international esaform conference on material forming: ESAFORM 2019. AIP Publishing, pp

2–8

46. Wang K, Addiego F, Bahlouli N, et al (2014) Impact response of recycled polypropylene-based composites under a wide range of temperature: Effect of filler content and recycling. Compos Sci Technol 95:89–99. https://doi.org/10.1016/j.compscitech.2014.02.014

47. Walley SM, Field JE, Pope R, Safford NA (1991) The rapid deformation behaviour of various polymers. J Phys III 1:1889–1925. https://doi.org/10.1051/jp3:1991240

48. Walley SM, Field JE, Pope PH, Safford NA (1989) A Study of the Rapid Deformation Behaviour of a Range of Polymers. Philos Trans R Soc A Math Phys Eng Sci 328:1–33. https://doi.org/10.1098/rsta.1989.0020

49. O'Connor C, Martin P, Menary G, et al (2011) Development of a Constitutive Model of Polypropylene for Thermoforming. In: The 14th International ESAFORM Conference on Material Forming: ESAFORM 2011. pp 874–879

50. Zrida M, Laurent H, Rio G, et al (2009) Experimental and numerical study of polypropylene behavior using an hyper-visco-hysteresis constitutive law. Comput Mater Sci 45:516–527. https://doi.org/10.1016/j.commatsci.2008.11.017

51. Drozdov AD, Gupta RK (2003) Non-linear viscoelasticity and viscoplasticity of isotactic polypropylene. Int J Eng Sci 41:2335–2361. https://doi.org/10.1016/S0020-7225(03)00239-8

52. Balieu R, Lauro F, Bennani B, et al (2013) A fully coupled elastoviscoplastic damage model at finite strains for mineral filled semi-crystalline polymer. Int J Plast 51:241–270. https://doi.org/10.1016/j.ijplas.2013.05.002

53. Okereke MI, Akpoyomare AI (2019) Two-process constitutive model for semicrystalline polymers across a wide range of strain rates. Polymer (Guildf) 183:121818. https://doi.org/10.1016/j.polymer.2019.121818

54. Pieczyska EA, Pęcherski RB, Gadaj SP, et al (2006) Experimental and theoretical investigations of glass-fibre reinforced composite subjected to uniaxial compression for a wide spectrum of strain rates. Arch Mech Warszawa 58:273–291

55. Nowak Z, Pecherski RB (2002) Plastic strain in metals by shear banding. II. Numerical identification and verification of plastic flow law accounting for shear banding. Arch Mech Warszawa 54:621–634

56. Cowper GR, Symonds PS (1957) Strain hardening and strain-rate effects in the impact

loading of cantilever beams. Tech Rep, Brown Univ Div Appl Math 1–46

57. Deng Y, Wang J, Yi P, et al (2018) Numerical Studies on Size Effect Behaviors of Glassy Polymers Based on Strain Gradient Elastoviscoplastic Model. J Appl Mech 86:021001. https://doi.org/10.1115/1.4041765

58. Yoon JW, Yang DY, Chung K, Barlat F (1999) A general elasto-plastic finite element formulation based on incremental deformation theory for planar anisotropy and its application to sheet metal forming. Int J Plast 15:35–67. https://doi.org/10.1016/s0749-6419(98)00059-x

59. Rossi M, Lattanzi A, Cortese L, Amodio D (2021) An approximated computational method for fast stress reconstruction in large strain plasticity. Int J Numer Methods Eng 121:1–18. https://doi.org/10.1002/nme.6346

60. Hibbitt H, Karlsson B, Sorensen E (2006) ABAQUS Theory Manual and Users' Manual, Version 6.6. Rhode Island, USA